A fully no-sampling formulation of the linear sampling method for three-dimensional inverse electromagnetic scattering problems

M Brignone[1] G Bozza[2] R Aramini[3] M Pastorino[2] and M Piana[1] §

[1] Dipartimento di Informatica, Università di Verona, Ca` Vignal 2, Strada le Grazie 15, 37134 Verona, Italy

[2] Dipartimento di Ingegneria Biofisica ed Elettronica, Università di Genova, via Opera Pia 11a, 16145 Genova, Italy

[3] Dipartimento di Ingegneria e Scienza dell'Informazione, Università di Trento, via Sommarive 14, 38050 Povo di Trento, Italy

Abstract. We describe a very fast and automatic formulation of the linear sampling method for three-dimensional electromagnetic inverse scattering problems. This formulation is an extension of a no-sampling implementation recently proposed for two-dimensional configurations. In this 3D framework, regularization occurs independently not only of the sampling point but even of the polarization of the fundamental solution used as known term. Furthermore, a very effective automatic procedure for the selection of the optimal surface describing the scatterer is introduced.

1. Introduction

The linear sampling method [9, 15] is a well-known numerical procedure for visualizing obstacles and inhomogeneous scatterers from measurements of acoustic or electromagnetic far-field patterns. At the basis of the method there is the regularized solution of the discretized and noisy version of a linear integral equation of the first kind, called the *far-field equation*, for each point of a computational grid set in a region containing the scatterer. The linear sampling method is a qualitative method [4] providing a reconstruction of the location and shape of the scatterer, but not providing quantitative information on the point values of the refractive index. Its main advantages are that, to be implemented, it does not need any a priori information on the scatterer (except that it is located inside a known bounded region); it has very wide applicability conditions, since it can be formulated in very general acoustic or electromagnetic

§ To whom correspondence should be addressed.

frameworks, in the case of two-dimensional and three-dimensional configurations, in the presence of both isotropic and anisotropic scatterers [4, 8, 11, 12, 13, 14, 15]; it is computationally more effective than methods like non-linear optimization techniques, which are often applied to inverse scattering problems.

In two recent papers, an augmented formulation of the method has been proposed, enhancing both the rapidity of the visualization process and the overall degree of automation of the algorithm. In fact in [1] the method is formulated in a direct sum of L^2 spaces, so that the traditional one-parameter family of integral equations of the first kind defined by the far-field equation is replaced by a single linear functional equation. In this approach, from now on called *no-sampling linear sampling*, a single regularization procedure is applied to the functional equation (in particular, a single regularization parameter is selected by means of some optimality criterion) and therefore the computation of the method is notably faster. In [2] an edge detection algorithm is applied to no-sampling linear sampling in order to provide an automatic and optimal selection of the edges of the map visualized by the qualitative method. The resulting algorithm is able to visualize the profile of the scatterer in a fast and automatic manner from the far-field data.

However, these two papers deal with two-dimensional inverse scattering problems. In the present paper we want to extend this no-sampling automatic formulation to a three-dimensional anisotropic electromagnetic inverse scattering problem. To this aim, two important critical issues must be accounted for. In the traditional implementation of the linear sampling method for Maxwell's equations, the regularized solution of the far-field equation depends on both the sampling point and the sampling polarization of the fundamental solution. Therefore, in principle, a different regularization parameter should be selected not only for each point of a computational grid in a volume containing the scatterer, but also for each vector in a set of polarizations. To avoid such increase of the computational effort, heuristic procedures can be introduced, although in [7] it is pointed out that the reconstruction depends on the choice of the polarization vector: in particular, in [7, 8] it is observed that the best visualizations are obtained by combining (with the same weight) the three indicator functions computed for three independent polarizations. The unifying approach followed in this paper allows replacing the two-parameters family of far-field equations with a single functional equation whose regularization occurs independently of both the sampling point and the sampling polarization, thus removing any problem in choosing the number and/or the distance of the sampling points, as well as in selecting the sampling polarizations and combining the corresponding indicator functions.

The second technical issue is concerned with the optimal selection of the scatterer surface. In linear sampling a point on the boundary induces the norm of the regularized solution of the far-field equation to grow up. In [2], in a two-dimensional setting, an

edge detection technique to highlight the contour of the scatterer is realized by means of deformable models. In principle, this technique could be extended to surfaces in 3D but, although active contours are reasonably fast, active surfaces [6] require a notable computational effort to converge to the boundary of the scatterer. The result of this procedure would be that the time saved by using the no-sampling implementation would be partly lost by the visualization process based on deformable volumes. Therefore in the present paper we prefer a different approach: the indicator function is restricted to an appropriate plane in $\mathbb{R}^3$ and the points of the scatterer surface belonging to this plane are determined by applying a 2D deformable model, just as in [2]. Then we compute the average value of the indicator function over this profile and the result is chosen as the threshold value setting a level surface of the indicator function which is used to visualize the boundary of the scatterer. This method is easily adapted to the case in which a non-connected scatterer consists of connected components characterized by different physical parameters: it suffices to consider restrictions of the indicator function to regions containing only one connected component and to select a different cut-off value for each region.

Summarizing, we present here a visualization method for 3D electromagnetic inverse scattering where no sampling is performed over the volume points or the polarization vectors and the profile of the scatterer is detected by means of an effective automatic thresholding of an analytically known indicator function. The result is an extremely fast algorithm: objects that are reconstructed in around half an hour by traditional linear sampling on a PC equipped with a 1.6 GHz processor and 1 GB RAM, are reconstructed with comparable accuracy by this fully no-sampling automatic procedure in around one minute.

The plan of the paper is as follows. In Section 2 we shortly summarize some results of [8], i.e. we introduce the far-field equation and recall the general theorem concerned with its approximate solution. In Section 3 we perform a rather general discretization of the far-field equation (the meshes in which the incidence and the observation directions are discretized do not need to be uniform or equal to each other) and provide the traditional formulation of the linear sampling method. Section 4 introduces the new formulation: with respect to [1], the generalization consists not only in passing from a 2D to a 3D framework and taking into account the sampling polarizations, but also in considering more general discretization meshes. Section 5 exploits the computational tools provided by [2] to perform some numerical examples illustrating the notable effectiveness of the new approach. Our conclusions are offered in Section 6.

2. The far-field equation

A very general electromagnetic inverse scattering problem [8, 10] is concerned with an incident time-harmonic field $\vec{E}^i = \vec{E}^i(\vec{x})$, entire solution of

$$\text{curl curl } \vec{E}^i(\vec{x}) - k^2 \vec{E}^i(\vec{x}) = 0, \qquad \vec{x} \in \mathbb{R}^3, \tag{2.1}$$

scattering against an inhomogeneous and possibly anisotropic target, whose support is represented, in a Cartesian coordinate system, by a bounded domain $\overline{D} \subset \mathbb{R}^3$, such that D is an open and Lipschitz domain of $\mathbb{R}^3$ with connected complement. The physical properties of the scatterer are described by a 3×3 symmetric matrix $N = N(\vec{x})$ (representing the possibly anisotropic index of refraction), whose entries are bounded complex-valued functions defined in $\mathbb{R}^3$ and such that N is the identity matrix outside $\overline{D}$. The relationship between the scatterer and the total electric field $\vec{E} = \vec{E}(\vec{x})$ is expressed by the equation

$$\text{curl curl } \vec{E}(\vec{x}) - k^2 N(\vec{x})\, \vec{E}(\vec{x}) = 0, \qquad \vec{x} \in \mathbb{R}^3, \tag{2.2}$$

where

$$\vec{E}(\vec{x}) = \vec{E}^s(\vec{x}) + \vec{E}^i(\vec{x}), \qquad \vec{x} \in \mathbb{R}^3, \tag{2.3}$$

and the scattered field $\vec{E}^s = \vec{E}^s(\vec{x})$ satisfies the Silver-Müller radiation condition

$$\lim_{|\vec{x}| \to \infty} \left(\text{curl } \vec{E}^s \times \vec{x} - \mathrm{i}k|\vec{x}| \vec{E}^s \right) = 0 \tag{2.4}$$

uniformly in $\hat{x} = \frac{\vec{x}}{|\vec{x}|}$.

In the following we shall assume that the electric incident field is a plane wave propagating along the direction $\hat{d}$ and polarized along $\vec{p} \in \mathbb{R}^3$ ($\vec{p} \cdot \hat{d} = 0$), i.e.

$$\vec{E}^i(\vec{x}) = \vec{p}\, e^{\mathrm{i}k\vec{x}\cdot\hat{d}}, \qquad \vec{x} \in \mathbb{R}^3. \tag{2.5}$$

The Stratton-Chu formula [10] implies that the radiating solutions $\vec{E}^s$ to the scattering problem have the asymptotic behavior

$$\vec{E}^s(\vec{x}) = \frac{e^{\mathrm{i}kr}}{r} \left\{ \vec{E}_\infty(\hat{x}; \hat{d}, \vec{p}) + \mathcal{O}\left(\frac{1}{r}\right) \right\} \qquad \text{as } r = |\vec{x}| \to \infty, \tag{2.6}$$

where the far-field pattern $\vec{E}_\infty(\cdot; \hat{d}, \vec{p})$ is defined on the unit sphere $\Omega := \{\vec{x} \in \mathbb{R}^3,\ |\vec{x}| = 1\}$. It is worth noting that $\vec{E}_\infty(\cdot; \hat{d}, \vec{p})$ is a tangential vector field, i.e. it belongs to $L_t^2(\Omega) := \{\vec{f}(\cdot) \in (L^2(\Omega))^3 \mid \vec{f}(\hat{x}) \cdot \vec{\nu}(\hat{x}) = 0\ \forall\, \hat{x} \in \Omega\}$, where $\vec{\nu}(\hat{x})$ is the normal unit vector to Ω in $\hat{x}$ and $\vec{f}(\hat{x}) \cdot \vec{\nu}(\hat{x})$ is the usual scalar product in $\mathbb{C}^3$ between $\vec{f}(\hat{x})$ and $\vec{\nu}(\hat{x})$. The set of functions $L_t^2(\Omega)$ is a Hilbert space with the scalar product defined by

$$\left(\vec{f}_1(\cdot)\,,\, \vec{f}_2(\cdot) \right)_{L_t^2(\Omega)} := \int_\Omega \vec{f}_1(\hat{d}) \cdot \vec{f}_2(\hat{d})\, ds(\hat{d}) \quad \forall\, \vec{f}_1(\cdot), \vec{f}_2(\cdot) \in L_t^2(\Omega). \tag{2.7}$$

Let us now introduce the *far-field equation* in the unknown $\vec{g}_{\vec{z},\vec{q}}(\cdot)$ for the 3D vector case [8]:

$$\int_\Omega \vec{E}_\infty(\hat{x};\hat{d},\vec{g}_{\vec{z},\vec{q}}(\hat{d}))ds(\hat{d}) = \vec{E}_{e,\infty}(\hat{x};\vec{z},\vec{q}). \tag{2.8}$$

Here $\vec{z}$ and $\vec{q}$ are respectively the sampling point in $\mathbb{R}^3$ and the sampling polarization; $\vec{E}_\infty(\hat{x};\hat{d},\vec{g}_{\vec{z},\vec{q}}(\hat{d}))$ denotes the far-field pattern of the field scattered by the target along direction $\hat{x}$ when it is illuminated by a plane wave impinging from direction $\hat{d}$ and polarized along $\vec{g}_{\vec{z},\vec{q}}(\hat{d})$; the function $\vec{g}_{\vec{z},\vec{q}}(\cdot)$ is in $L^2_t(\Omega)$ for each $\vec{z} \in \mathbb{R}^3$ and $\vec{q} \in \mathbb{R}^3$; finally, $\vec{E}_{e,\infty}(\hat{x};\vec{z},\vec{q})$ is the far-field pattern of an elementary dipole located in $\vec{z}$ and oriented along $\vec{q}$:

$$\vec{E}_{e,\infty}(\hat{x};\vec{z},\vec{q}) := \frac{\mathrm{i}k}{4\pi}(\hat{x}\times\vec{q})\times\hat{x}\; e^{-\mathrm{i}k\hat{x}\cdot\vec{z}}. \tag{2.9}$$

We now observe that, owing to the linear dependence of the far-field patterns on the polarizations (see, e.g., (2.9)) and to the linearity of the far-field equation (2.8), we do not loose in generality by assuming $|\vec{q}| = 1$; hence in the following we shall consider $\vec{q} = \hat{q} \in \Omega$. Then, if we introduce the *far-field operator* $F : L^2_t(\Omega) \to L^2_t(\Omega)$ defined by

$$\left(F\vec{g}(\cdot)\right)(\hat{x}) := \int_\Omega \vec{E}_\infty(\hat{x};\hat{d},\vec{g}(\hat{d}))ds(\hat{d}), \tag{2.10}$$

the far-field equation (2.8) can be written as

$$\left(F\vec{g}_{\vec{z},\hat{q}}(\cdot)\right)(\hat{x}) = \vec{E}_{e,\infty}(\hat{x};\vec{z},\hat{q}). \tag{2.11}$$

At the basis of the linear sampling method there is the following *general theorem* [8].

Theorem 2.1 (general theorem). *Let us assume that k is not a transmission eigenvalue and let F be the far-field operator* (2.10)*; moreover, let $\hat{q}$ be any element of Ω. Then we have:*
1) *if $\vec{z} \in D$, then for every $\epsilon > 0$ there exists a solution $\vec{g}_{\vec{z},\hat{q}}(\cdot) \in L^2_t(\Omega)$ of the inequality*

$$\|(F\vec{g}_{\vec{z},\hat{q}}(\cdot))(\cdot) - \vec{E}_{e,\infty}(\cdot;\vec{z},\hat{q})\|_{L^2_t(\Omega)} < \epsilon, \tag{2.12}$$

such that

$$\lim_{\vec{z}\to\partial D} \|\vec{g}_{\vec{z},\hat{q}}(\cdot)\|_{L^2_t(\Omega)} = \infty; \tag{2.13}$$

2) *if $\vec{z} \notin D$, then for every $\epsilon > 0$ and $\delta > 0$ there exists a solution $\vec{g}_{\vec{z},\hat{q}}(\cdot) \in L^2_t(\Omega)$ of the inequality*

$$\|(F\vec{g}_{\vec{z},\hat{q}}(\cdot))(\cdot) - \vec{E}_{e,\infty}(\cdot;\vec{z},\hat{q})\|_{L^2_t(\Omega)} < \epsilon + \delta, \tag{2.14}$$

such that

$$\lim_{\delta\to 0} \|\vec{g}_{\vec{z},\hat{q}}(\cdot)\|_{L^2_t(\Omega)} = \infty. \tag{2.15}$$

Analogous theorems hold for scattering problems formulated for conductors or partially coated objects: in addition to [8], see [4] and references therein.

3. Discretization and the linear sampling method

The aim of the present section is to perform an angular discretization of the far-field equation that allows one to deal with very general scattering situations, such as non-uniform displacement of the emitting and receiving antennas and limited aperture data. The first step towards such a discretization is to project the far-field patterns onto some particular basis. A possible choice is the spherical basis $\{\hat{r}(\hat{w}), \hat{\theta}(\hat{w}), \hat{\varphi}(\hat{w})\}$ (with $\hat{r}(\hat{w}) = \hat{w}$) intrinsic to the generic direction $\hat{w}$. Since the far-field pattern $\vec{E}_\infty(\cdot; \hat{d}, \vec{p})$ belongs to $L^2_t(\Omega)$, it has no component along $\hat{r}(\hat{x})$ and we can write

$$\vec{E}_\infty(\hat{x}; \hat{d}, \vec{p}) = E^\theta_\infty(\hat{x}; \hat{d}, \vec{p})\hat{\theta}(\hat{x}) + E^\varphi_\infty(\hat{x}; \hat{d}, \vec{p})\hat{\varphi}(\hat{x}), \tag{3.1}$$

where $E^\theta_\infty(\hat{x}; \hat{d}, \vec{p}) := \vec{E}_\infty(\hat{x}; \hat{d}, \vec{p}) \cdot \hat{\theta}(\hat{x})$ and $E^\varphi_\infty(\hat{x}; \hat{d}, \vec{p}) := \vec{E}_\infty(\hat{x}; \hat{d}, \vec{p}) \cdot \hat{\varphi}(\hat{x})$. Moreover, since $\vec{p} \cdot \hat{d} = 0$, then $\vec{p}$ can be decomposed as

$$\vec{p} = p^\theta \hat{\theta}(\hat{d}) + p^\varphi \hat{\varphi}(\hat{d}), \tag{3.2}$$

where $p^\theta := \vec{p} \cdot \hat{\theta}(\hat{d})$ and $p^\varphi := \vec{p} \cdot \hat{\varphi}(\hat{d})$. Hence, exploiting the linearity of the far-field pattern with respect to $\vec{p}$, it is possible to write

$$E^\theta_\infty(\hat{x}; \hat{d}, \vec{p}) = p^\theta E^{\theta\theta}_\infty(\hat{x}; \hat{d}) + p^\varphi E^{\theta\varphi}_\infty(\hat{x}; \hat{d}), \tag{3.3}$$

$$E^\varphi_\infty(\hat{x}; \hat{d}, \vec{p}) = p^\theta E^{\varphi\theta}_\infty(\hat{x}; \hat{d}) + p^\varphi E^{\varphi\varphi}_\infty(\hat{x}; \hat{d}), \tag{3.4}$$

where

$$E^{\theta\theta}_\infty(\hat{x}; \hat{d}) := E^\theta_\infty(\hat{x}; \hat{d}, \hat{\theta}(\hat{d})), \tag{3.5}$$

$$E^{\theta\varphi}_\infty(\hat{x}; \hat{d}) := E^\theta_\infty(\hat{x}; \hat{d}, \hat{\varphi}(\hat{d})), \tag{3.6}$$

$$E^{\varphi\theta}_\infty(\hat{x}; \hat{d}) := E^\varphi_\infty(\hat{x}; \hat{d}, \hat{\theta}(\hat{d})), \tag{3.7}$$

$$E^{\varphi\varphi}_\infty(\hat{x}; \hat{d}) := E^\varphi_\infty(\hat{x}; \hat{d}, \hat{\varphi}(\hat{d})). \tag{3.8}$$

Analogously to (3.1), the far-field pattern $\vec{E}_{e,\infty}(\cdot; \vec{z}, \hat{q}) \in L^2_t(\Omega)$, defined by (2.9), can be written in terms of $\hat{\theta}(\hat{x})$ and $\hat{\varphi}(\hat{x})$ as

$$\vec{E}_{e,\infty}(\hat{x}; \vec{z}, \hat{q}) = E^\theta_{e,\infty}(\hat{x}; \vec{z}, \hat{q})\hat{\theta}(\hat{x}) + E^\varphi_{e,\infty}(\hat{x}; \vec{z}, \hat{q})\hat{\varphi}(\hat{x}), \tag{3.9}$$

where $E^\theta_{e,\infty}(\hat{x}; \vec{z}, \hat{q}) := \vec{E}_{e,\infty}(\hat{x}; \vec{z}, \hat{q}) \cdot \hat{\theta}(\hat{x})$ and $E^\varphi_{e,\infty}(\hat{x}; \vec{z}, \hat{q}) := \vec{E}_{e,\infty}(\hat{x}; \vec{z}, \hat{q}) \cdot \hat{\varphi}(\hat{x})$. As a consequence, the vector equation (2.11) can be split into two scalar ones:

$$\left(F\vec{g}_{\vec{z},\hat{q}}(\cdot)\right)(\hat{x}) \cdot \hat{\theta}(\hat{x}) = E^\theta_{e,\infty}(\hat{x}; \vec{z}, \hat{q}), \tag{3.10}$$

$$\left(F\vec{g}_{\vec{z},\hat{q}}(\cdot)\right)(\hat{x}) \cdot \hat{\varphi}(\hat{x}) = E^\varphi_{e,\infty}(\hat{x}; \vec{z}, \hat{q}), \tag{3.11}$$

i.e., recalling definition (2.10) and decompositions (3.1), (3.3), (3.4),

$$\int_\Omega [g^\theta_{\vec{z},\hat{q}}(\hat{d}) E^{\theta\theta}_\infty(\hat{x};\hat{d}) + g^\varphi_{\vec{z},\hat{q}}(\hat{d}) E^{\theta\varphi}_\infty(\hat{x};\hat{d})]\, ds(\hat{d}) = E^\theta_{e,\infty}(\hat{x};\vec{z},\hat{q}), \tag{3.12}$$

$$\int_\Omega [g^\theta_{\vec{z},\hat{q}}(\hat{d}) E^{\varphi\theta}_\infty(\hat{x};\hat{d}) + g^\varphi_{\vec{z},\hat{q}}(\hat{d}) E^{\varphi\varphi}_\infty(\hat{x};\hat{d})]\, ds(\hat{d}) = E^\varphi_{e,\infty}(\hat{x};\vec{z},\hat{q}). \tag{3.13}$$

In real experiments, the far-field pattern is measured for $L_{\hat{x}} = T_{\hat{x}} F_{\hat{x}}$ observation directions and $L_{\hat{d}} = T_{\hat{d}} F_{\hat{d}}$ incidence directions. The observation directions are denoted as

$$\hat{x}_{\ell_{\hat{x}}(i,j)} = (\sin\theta^{\hat{x}}_i \cos\varphi^{\hat{x}}_j\,,\, \sin\theta^{\hat{x}}_i \sin\varphi^{\hat{x}}_j\,,\, \cos\theta^{\hat{x}}_i) \in \Omega, \tag{3.14}$$

where, for all integers $i = 0,\ldots,T_{\hat{x}}-1$ and $j = 0,\ldots,F_{\hat{x}}-1$, we have put

$$\ell_{\hat{x}}(i,j) := iF_{\hat{x}} + j, \quad \theta^{\hat{x}}_i \in (0;\pi), \quad \varphi^{\hat{x}}_j \in [0,2\pi); \tag{3.15}$$

analogously, the incidence directions are denoted as

$$\hat{d}_{\ell_{\hat{d}}(i,j)} = (\sin\theta^{\hat{d}}_i \cos\varphi^{\hat{d}}_j\,,\, \sin\theta^{\hat{d}}_i \sin\varphi^{\hat{d}}_j\,,\, \cos\theta^{\hat{d}}_i) \in \Omega, \tag{3.16}$$

where, for all integers $i = 0,\ldots,T_{\hat{d}}-1$ and $j = 0,\ldots,F_{\hat{d}}-1$, we have put

$$\ell_{\hat{d}}(i,j) := iF_{\hat{d}} + j, \quad \theta^{\hat{d}}_i \in (0,\pi), \quad \varphi^{\hat{d}}_j \in [0,2\pi). \tag{3.17}$$

As a consequence, equations (3.12) and (3.13) can be discretized by requiring that, for all $\ell_{\hat{x}} = 0,\ldots,L_{\hat{x}}-1$,

$$\sum_{\ell_{\hat{d}}=0}^{L_{\hat{d}}-1} [g^\theta_{\vec{z},\hat{q}}(\hat{d}_{\ell_{\hat{d}}}) E^{\theta\theta}_\infty(\hat{x}_{\ell_{\hat{x}}};\hat{d}_{\ell_{\hat{d}}}) + g^\varphi_{\vec{z},\hat{q}}(\hat{d}_{\ell_{\hat{d}}}) E^{\theta\varphi}_\infty(\hat{x}_{\ell_{\hat{x}}};\hat{d}_{\ell_{\hat{d}}})]\, \Delta s_{\ell_{\hat{d}}} = E^\theta_{e,\infty}(\hat{x}_{\ell_{\hat{x}}};\vec{z},\hat{q}), \tag{3.18}$$

$$\sum_{\ell_{\hat{d}}=0}^{L_{\hat{d}}-1} [g^\theta_{\vec{z},\hat{q}}(\hat{d}_{\ell_{\hat{d}}}) E^{\varphi\theta}_\infty(\hat{x}_{\ell_{\hat{x}}};\hat{d}_{\ell_{\hat{d}}}) + g^\varphi_{\vec{z},\hat{q}}(\hat{d}_{\ell_{\hat{d}}}) E^{\varphi\varphi}_\infty(\hat{x}_{\ell_{\hat{x}}};\hat{d}_{\ell_{\hat{d}}})]\, \Delta s_{\ell_{\hat{d}}} = E^\varphi_{e,\infty}(\hat{x}_{\ell_{\hat{x}}};\vec{z},\hat{q}), \tag{3.19}$$

where, for all $i = 0,\ldots,T_{\hat{d}}-1$ and $j = 0,\ldots,F_{\hat{d}}-1$, we have defined

$$\Delta s_{\ell_{\hat{d}}} := \sin\theta^{\hat{d}}_i \Delta\theta^{\hat{d}}_i \Delta\varphi^{\hat{d}}_j > 0, \tag{3.20}$$

with $\Delta\theta^{\hat{d}}_i := \theta^{\hat{d}}_{i+1} - \theta^{\hat{d}}_i > 0$ and $\Delta\varphi^{\hat{d}}_j := \varphi^{\hat{d}}_{j+1} - \varphi^{\hat{d}}_j > 0$. In particular, in the case of uniform discretization we have $\Delta\theta^{\hat{d}}_i = \pi/T_{\hat{d}}$ and $\Delta\varphi^{\hat{d}}_j = 2\pi/F_{\hat{d}}$.

Equations (3.18) and (3.19) can be written in a more compact form by using the matrix notation:

$$\mathbf{E}_\infty\, \mathbf{\Delta S}_{\hat{d}}\, \mathbf{G}_{\vec{z},\hat{q}} = \mathbf{E}_{e,\infty}(\vec{z},\hat{q}), \tag{3.21}$$

where we have defined $\mathbf{\Delta S}_{\hat{d}}$ as the diagonal and positive-definite matrix of $2L_{\hat{d}} \times 2L_{\hat{d}}$ elements

$$\mathbf{\Delta S}_{\hat{d}} := \begin{pmatrix} \mathbf{\Delta s}_{\hat{d}} & \mathbf{0} \\ \mathbf{0} & \mathbf{\Delta s}_{\hat{d}} \end{pmatrix} \tag{3.22}$$

with $\mathbf{\Delta s}_{\hat{d}} := \mathrm{diag}\left(\Delta s_{\ell_{\hat{d}}}\right)_{\ell_{\hat{d}}=0,\dots,L_{\hat{d}}-1}$; $\mathbf{G}_{\vec{z},\hat{q}}$ as the column vector of length $2L_{\hat{d}}$

$$\mathbf{G}_{\vec{z},\hat{q}} := \begin{pmatrix} \mathbf{g}^{\theta}_{\vec{z},\hat{q}} \\ \mathbf{g}^{\varphi}_{\vec{z},\hat{q}} \end{pmatrix} \tag{3.23}$$

with $\mathbf{g}^{\theta}_{\vec{z},\hat{q}} := \left(g^{\theta}_{\vec{z},\hat{q}}(\hat{d}_{\ell_{\hat{d}}})\right)_{\ell_{\hat{d}}=0,\dots,L_{\hat{d}}-1}$, $\mathbf{g}^{\varphi}_{\vec{z},\hat{q}} := \left(g^{\varphi}_{\vec{z},\hat{q}}(\hat{d}_{\ell_{\hat{d}}})\right)_{\ell_{\hat{d}}=0,\dots,L_{\hat{d}}-1}$; $\mathbf{E}_{e,\infty}(\vec{z},\hat{q})$ as the column vector of length $2L_{\hat{x}}$

$$\mathbf{E}_{e,\infty}(\vec{z},\hat{q}) := \begin{pmatrix} \mathbf{E}^{\theta}_{e,\infty}(\vec{z},\hat{q}) \\ \mathbf{E}^{\varphi}_{e,\infty}(\vec{z},\hat{q}) \end{pmatrix} \tag{3.24}$$

with $\mathbf{E}^{\theta}_{e,\infty}(\vec{z},\hat{q}) := \left(E^{\theta}_{e,\infty}(\hat{x}_{\ell_{\hat{x}}};\vec{z},\hat{q})\right)_{\ell_{\hat{x}}=0,\dots,L_{\hat{x}}-1}$, $\mathbf{E}^{\varphi}_{e,\infty}(\vec{z},\hat{q}) := \left(E^{\varphi}_{e,\infty}(\hat{x}_{\ell_{\hat{x}}};\vec{z},\hat{q})\right)_{\ell_{\hat{x}}=0,\dots,L_{\hat{x}}-1}$; finally, the $2L_{\hat{x}} \times 2L_{\hat{d}}$ matrix $\mathbf{E}_{\infty}$ is defined as

$$\mathbf{E}_{\infty} := \begin{pmatrix} \mathbf{E}^{\theta\theta}_{\infty} & \mathbf{E}^{\theta\varphi}_{\infty} \\ \mathbf{E}^{\varphi\theta}_{\infty} & \mathbf{E}^{\varphi\varphi}_{\infty} \end{pmatrix} \tag{3.25}$$

with

$$\begin{aligned}
\mathbf{E}^{\theta\theta}_{\infty} &:= \left(E^{\theta\theta}_{\infty}(\hat{x}_{\ell_{\hat{x}}};\hat{d}_{\ell_{\hat{d}}})\right)_{\ell_{\hat{x}}=0,\dots,L_{\hat{x}}-1;\ell_{\hat{d}}=0,\dots,L_{\hat{d}}-1}, \\
\mathbf{E}^{\theta\varphi}_{\infty} &:= \left(E^{\theta\varphi}_{\infty}(\hat{x}_{\ell_{\hat{x}}};\hat{d}_{\ell_{\hat{d}}})\right)_{\ell_{\hat{x}}=0,\dots,L_{\hat{x}}-1;\ell_{\hat{d}}=0,\dots,L_{\hat{d}}-1}, \\
\mathbf{E}^{\varphi\theta}_{\infty} &:= \left(E^{\varphi\theta}_{\infty}(\hat{x}_{\ell_{\hat{x}}};\hat{d}_{\ell_{\hat{d}}})\right)_{\ell_{\hat{x}}=0,\dots,L_{\hat{x}}-1;\ell_{\hat{d}}=0,\dots,L_{\hat{d}}-1}, \\
\mathbf{E}^{\varphi\varphi}_{\infty} &:= \left(E^{\varphi\varphi}_{\infty}(\hat{x}_{\ell_{\hat{x}}};\hat{d}_{\ell_{\hat{d}}})\right)_{\ell_{\hat{x}}=0,\dots,L_{\hat{x}}-1;\ell_{\hat{d}}=0,\dots,L_{\hat{d}}-1}.
\end{aligned}$$

Remark 3.1. The positive-definite matrix $\mathbf{\Delta S}_{\hat{d}}$ given in (3.22) defines a (weighted) scalar product $(\cdot,\cdot)_{L_{\hat{d}}}$ in $\mathbb{C}^{2L_{\hat{d}}}$, obtained from a $L_{\hat{d}}-$angular discretization of the scalar product (2.7). If $\mathbf{w}_1$ and $\mathbf{w}_2$ are two column vectors in $\mathbb{C}^{2L_{\hat{d}}}$, we have

$$(\mathbf{w}_1,\mathbf{w}_2)_{L_{\hat{d}}} := \mathbf{w}_1^{\mathrm{T}}\mathbf{\Delta S}_{\hat{d}}\,\overline{\mathbf{w}}_2, \tag{3.26}$$

where $\mathbf{w}_1^{\mathrm{T}}$ denotes the transpose of $\mathbf{w}_1$ and $\overline{\mathbf{w}}_2$ the complex conjugate of $\mathbf{w}_2$. The scalar product (3.26) induces a norm, denoted with $\|\cdot\|_{L_{\hat{d}}}$, in $\mathbb{C}^{2L_{\hat{d}}}$; we shall write $\left(\mathbb{C}^{2L_{\hat{d}}},(\cdot,\cdot)_{L_{\hat{d}}}\right)$ to denote the vector space $\mathbb{C}^{2L_{\hat{d}}}$ endowed with the scalar product $(\cdot,\cdot)_{L_{\hat{d}}}$. In a completely analogous way, we can consider the space $\left(\mathbb{C}^{2L_{\hat{x}}},(\cdot,\cdot)_{L_{\hat{x}}}\right)$, by simply replacing the weight matrix (3.22) with its analogous $\mathbf{\Delta S}_{\hat{x}}$, defined in terms of $\Delta s_{\ell_{\hat{x}}} := \sin\theta_i^{\hat{x}}\Delta\theta_i^{\hat{x}}\Delta\varphi_j^{\hat{x}} > 0$.

In real applications, the far-field patterns are blurred by the noise affecting the measurement processes, so that only a noisy version $\mathbf{E}^{\mathbf{H}}_{\infty}$ of the far-field patterns is available, i.e.

$$\mathbf{E}^{\mathbf{H}}_{\infty} := \mathbf{E}_{\infty} + \mathbf{H}, \tag{3.27}$$

where $\mathbf{H}$ is the noise matrix. Then, we can define the linear operator

$$\begin{array}{rcl} \mathcal{F}^h : \left(\mathbb{C}^{2L_{\hat{d}}}, (\cdot,\cdot)_{L_{\hat{d}}}\right) & \rightarrow & \left(\mathbb{C}^{2L_{\hat{x}}}, (\cdot,\cdot)_{L_{\hat{x}}}\right) \\ \mathbf{x} & \mapsto & \mathbf{E}^{\mathbf{H}}_{\infty}\, \boldsymbol{\Delta}\mathbf{S}_{\hat{d}}\, \mathbf{x}; \end{array} \tag{3.28}$$

h is used as a superscript to distinguish $\mathcal{F}^h$ from the corresponding noise-free version $\mathcal{F}$ and also to denote the noise bound $h \geq \|\mathcal{F}^h - \mathcal{F}\|$, where $\|\cdot\|$ indicates the operator norm. By virtue of (3.28), $\mathbf{E}^{\mathbf{H}}_{\infty}\, \boldsymbol{\Delta}\mathbf{S}_{\hat{d}} =: \mathbf{F}^h$ is the matrix representation of the linear operator $\mathcal{F}^h$; moreover, remembering (3.21), we can now write the noisy and discretized version of the far-field equation (2.8) in the form:

$$\mathbf{F}^h \mathbf{G}_{\vec{z},\hat{q}} = \mathbf{E}_{e,\infty}(\vec{z},\hat{q}). \tag{3.29}$$

The ill-conditioning of equation (3.29) requires a regularization procedure; in particular, Tikhonov regularization method [17] consists in determining

$$\mathbf{G}_{\vec{z},\hat{q};\,\alpha} = \mathrm{argmin}_{\mathbf{G}\in\mathbb{C}^{2L_{\hat{d}}}} \left\{ \left\| \mathbf{F}^h\mathbf{G} - \mathbf{E}_{e,\infty}(\vec{z},\hat{q}) \right\|^2_{L_{\hat{x}}} + \alpha \left\|\mathbf{G}\right\|^2_{L_{\hat{d}}} \right\}. \tag{3.30}$$

Given (3.30), the optimal regularized solution is obtained by choosing for the regularization parameter α the value $\alpha^*(\vec{z},\hat{q})$ determined by the generalized discrepancy principle, i.e. by finding the zero of the generalized discrepancy function $\rho : (0,+\infty) \rightarrow \mathbb{R}$ defined as [17]

$$\rho(\alpha) := \left\| \mathbf{F}^h \mathbf{G}_{\vec{z},\hat{q};\,\alpha} - \mathbf{E}_{e,\infty}(\vec{z},\hat{q}) \right\|^2_{L_{\hat{x}}} - h^2 \left\|\mathbf{G}_{\vec{z},\hat{q};\,\alpha}\right\|^2_{L_{\hat{d}}}. \tag{3.31}$$

An explicit form for this regularized solution can be determined by using the singular representation [3, 10] of the linear operator $\mathcal{F}^h$, whose singular system is related to that of the matrix $\mathbf{F}^h$ according to Theorem A.1 in the Appendix. If we denote with $\{\sigma^h_p, \mathbf{u}^h_p, \mathbf{v}^h_p\}_{p=0}^{r^h-1}$ (where $\sigma^h_0 \geq \sigma^h_1 \geq \ldots \geq \sigma^h_{r^h-1}$ and $r^h := \mathrm{rank}\,\mathbf{F}^h$) the singular system of $\mathcal{F}^h$ and if $\alpha^*(\vec{z},\hat{q})$ is the zero of the generalized discrepancy function (3.31), it turns out that the optimal Tikhonov regularized solution of (3.29) is given by [3, 10]:

$$\mathbf{G}_{\vec{z},\hat{q};\,\alpha^*(\vec{z},\hat{q})} = \sum_{p=0}^{r^h-1} \frac{\sigma^h_p}{(\sigma^h_p)^2 + \alpha^*(\vec{z},\hat{q})} \left(\mathbf{E}_{e,\infty}(\vec{z},\hat{q}), \mathbf{v}^h_p\right)_{L_{\hat{x}}} \mathbf{u}^h_p. \tag{3.32}$$

Then, inspired by Theorem 2.1, the linear sampling method allows one to visualize the scatterer profile by performing the following steps:

- take a grid of points $\mathcal{Z} \subset \mathbb{R}^3$ covering the scatterer and choose a sampling polarization $\hat{q}$;
- for each grid point $\vec{z} \in \mathcal{Z}$, determine the optimal Tikhonov regularized solution (3.32);
- for each grid point $\vec{z} \in \mathcal{Z}$, consider the quantity $\left\|\mathbf{G}_{\vec{z},\hat{q};\,\alpha^*(\vec{z},\hat{q})}\right\|_{L_{\hat{d}}}$ or a suitable combination of the analogous quantities obtained for different choices of $\hat{q}$ [8];

- visualize the profile of the scatterer as the set of grid points in which the previous combination becomes mostly large or small, depending on the analytical form chosen for the combination itself.

It is worth noting that $\left\|\mathbf{G}_{\vec{z},\hat{q};\,\alpha^*(\vec{z},\hat{q})}\right\|^2_{L_{\hat{d}}}$ can be explicitly computed, by using (3.32), as

$$\left\|\mathbf{G}_{\vec{z},\hat{q};\,\alpha^*(\vec{z},\hat{q})}\right\|^2_{L_{\hat{d}}} = \sum_{p=0}^{r^h-1} \frac{(\sigma_p^h)^2}{\left[(\sigma_p^h)^2 + \alpha^*(\vec{z},\hat{q})\right]^2} \left|\left(\mathbf{E}_{e,\infty}(\vec{z},\hat{q}), \mathbf{v}_p^h\right)_{L_{\hat{x}}}\right|^2. \tag{3.33}$$

In this implementation the optimal regularization parameter $\alpha^*(\vec{z},\hat{q})$ explicitly depends on the grid point $\vec{z}$ and the prefixed $\hat{q}$ and therefore it must be computed a number of times equal to the product of the number of grid points times the number of polarizations sampled in Ω.

As a final remark, we point out that this discretization can be easily generalized to the case of limited aperture data. It suffices to consider $\theta_i^{\hat{d}} \in \left(\overline{\theta}_1^{\hat{d}}, \overline{\theta}_2^{\hat{d}}\right) \subset (0,\pi)$ for $i = 0,\ldots,T_{\hat{d}}-1$; $\varphi_j^{\hat{d}} \in \left[\overline{\varphi}_1^{\hat{d}}, \overline{\varphi}_2^{\hat{d}}\right) \subset [0,2\pi)$ for $j = 0,\ldots,F_{\hat{d}}-1$; $\theta_i^{\hat{x}} \in \left(\overline{\theta}_1^{\hat{x}}, \overline{\theta}_2^{\hat{x}}\right) \subset (0,\pi)$ for $i = 0,\ldots,T_{\hat{x}}-1$; $\varphi_j^{\hat{x}} \in \left[\overline{\varphi}_1^{\hat{x}}, \overline{\varphi}_2^{\hat{x}}\right) \subset [0,2\pi)$ for $j = 0,\ldots,F_{\hat{x}}-1$.

4. A no-sampling implementation of the linear sampling method

The key-idea of no-sampling is to replace the discrete grid $\mathcal{Z}$ with a continuous one $T := [-A_1,A_1] \times [-A_2,A_2] \times [-A_3,A_3] \subset \mathbb{R}^3$ and, furthermore, to replace a finite set of sampled polarizations with Ω. This approach, whose purpose is to increase the computational effectiveness and the automation degree of the traditional linear sampling method, amounts to regarding expression (3.33) as a sampled version of a function defined over $T \times \Omega$. The critical issue in this process is that, while the dependence of $\left\|\mathbf{G}_{\vec{z},\hat{q};\,\alpha^*(\vec{z},\hat{q})}\right\|^2_{L_{\hat{d}}}$ on $\vec{z}$ and $\hat{q}$ is explicitly known for the term $\mathbf{E}_{e,\infty}(\vec{z},\hat{q})$ (see (2.9), (3.9), (3.24), (3.33)), this is not true for the optimal value of the regularization parameter, since $\alpha^*(\vec{z},\hat{q})$ can only be computed numerically as the zero of the generalized discrepancy function (3.31). This problem can be solved by setting the formulation of the method in a new mathematical framework, which enables us to consider as a unique functional equation the infinitely many algebraic linear systems

$$\mathbf{F}^h\mathbf{G}(\vec{z},\hat{q}) = \mathbf{E}_{e,\infty}(\vec{z},\hat{q}) \qquad \forall \vec{z} \in T,\ \forall \hat{q} \in \Omega \tag{4.1}$$

that would arise from (3.29) if, with a "naive" procedure, the unknown vector $\mathbf{G}_{\vec{z},\hat{q}}$ were simply regarded as an unknown function $\mathbf{G}(\vec{z},\hat{q})$ of the continuous parameters $\vec{z}$ and $\hat{q}$.

The new mathematical setting requires the introduction of two functional spaces. Given the total number $L_{\hat{d}}$ of incidence directions, let us consider the Hilbert space

$[L^2(\mathcal{B})]^{2L_{\hat{d}}}$, where $\mathcal{B} := T \times \Omega$, equipped with the (weighted) scalar product

$$(\mathbf{f}(\cdot), \mathbf{g}(\cdot))_{2,L_{\hat{d}}} := \sum_{\ell_{\hat{d}}=0}^{L_{\hat{d}}-1} \Delta s_{\ell_{\hat{d}}} (f_{\ell_{\hat{d}}}(\cdot), g_{\ell_{\hat{d}}}(\cdot))_{L^2(\mathcal{B})} + \sum_{\ell_{\hat{d}}=0}^{L_{\hat{d}}-1} \Delta s_{\ell_{\hat{d}}} (f_{L_{\hat{d}}+\ell_{\hat{d}}}(\cdot), g_{L_{\hat{d}}+\ell_{\hat{d}}}(\cdot))_{L^2(\mathcal{B})} \quad (4.2)$$

for all $\mathbf{f}(\cdot) := \{f_t(\cdot)\}_{t=0}^{2L_{\hat{d}}-1}$, $\mathbf{g}(\cdot) := \{g_t(\cdot)\}_{t=0}^{2L_{\hat{d}}-1} \in [L^2(\mathcal{B})]^{2L_{\hat{d}}}$, where the weights $\Delta s_{\ell_{\hat{d}}}$ are defined in (3.20) and where $(\cdot,\cdot)_{L^2(\mathcal{B})}$ denotes the usual scalar product in $L^2(\mathcal{B})$; moreover, we shall denote by $\|\cdot\|_{2,L_{\hat{d}}}$ the induced norm, i.e.

$$\|\mathbf{f}(\cdot)\|_{2,L_{\hat{d}}} := \sqrt{\int_{\mathcal{B}} \|\mathbf{f}(\vec{z},\hat{q})\|_{L_{\hat{d}}}^2 \, d\vec{z}\, ds(\hat{q})}\,. \quad (4.3)$$

In a completely analogous way we can define the Hilbert space $[L^2(\mathcal{B})]^{2L_{\hat{x}}}$, where $L_{\hat{x}}$ is the total number of observation directions.

We can now introduce the following linear operator, whose aim is that of enabling the operator $\mathcal{F}^h$, defined in (3.28), to act on $2L_{\hat{d}}-$uples of functions, rather than on $2L_{\hat{d}}-$uples of complex numbers.

Definition 4.1: *The linear operator* $\mathsf{F}^h : [L^2(\mathcal{B})]^{2L_{\hat{d}}} \to [L^2(\mathcal{B})]^{2L_{\hat{x}}}$ *is defined as*

$$\left[\mathsf{F}^h \mathbf{G}(\cdot)\right](\cdot) := \left\{ \sum_{t=0}^{2L_{\hat{d}}-1} (\mathbf{F}^h)_{st}\, G_t(\cdot) \right\}_{s=0}^{2L_{\hat{x}}-1}, \quad (4.4)$$

where $\mathbf{G}(\cdot) := \{G_t(\cdot)\}_{t=0}^{2L_{\hat{d}}-1} \in [L^2(\mathcal{B})]^{2L_{\hat{d}}}$ *and* $(\mathbf{F}^h)_{st}$ *are the elements of the matrix* $\mathbf{F}^h$.

Theorem 4.2: *The following properties for the linear operator* F^h *hold:*

i) it is continuous, but not compact;

ii) its kernel $\mathcal{N}(\mathsf{F}^h)$ *is given by:*

$$\mathcal{N}(\mathsf{F}^h) = \left\{ \mathbf{G}(\cdot) \in \left[L^2(\mathcal{B})\right]^{2L_{\hat{d}}} \mid \mathbf{G}(\vec{z},\hat{q}) \in \mathcal{N}(\mathbf{F}^h) \text{ f.a.a. } (\vec{z},\hat{q}) \in \mathcal{B} \right\}; \quad (4.5)$$

iii) if $\mathbf{G}(\cdot) \in [L^2(\mathcal{B})]^{2L_{\hat{d}}}$ *is such that* $\mathbf{G}(\vec{z},\hat{q}) \in \mathcal{N}(\mathbf{F}^h)^{\perp}$ *for almost all* $(\vec{z},\hat{q}) \in \mathcal{B}$, *then* $\mathbf{G}(\cdot) \in \mathcal{N}(\mathsf{F}^h)^{\perp}$, *where the orthogonality must be intended with respect to the scalar product of the corresponding vector space.*

Proof. These properties can be proved in full analogy with Theorem 3.2 and Remark 3.3 in [1]. □

The non-compactness of F^h does not prevent us from using the singular representation of the linear operator $\mathcal{F}^h$. Hence, we obtain the following expression for F^h:

$$[\mathsf{F}^h\mathbf{G}(\cdot)](\cdot) = \left\{ \sum_{p=0}^{r^h-1} \sigma_p^h \, v_{p,s}^h \, (\mathbf{G}(\cdot), \mathbf{u}_p^h)_{L_{\hat{d}}} \right\}_{s=0}^{2L_{\hat{x}}-1} \quad \forall \mathbf{G}(\cdot) \in \left[L^2(\mathcal{B})\right]^{2L_{\hat{d}}}, \tag{4.6}$$

where $v_{p,s}^h$ is the s-th component of $\mathbf{v}_p^h$ and $(\mathbf{G}(\cdot), \mathbf{u}_p^h)_{L_{\hat{d}}}$ is defined as the element in $L^2(\mathcal{B})$ such that

$$(\mathbf{G}(\cdot), \mathbf{u}_p^h)_{L_{\hat{d}}} \, : \, \mathcal{B} \ni (\vec{z}, \hat{q}) \mapsto (\mathbf{G}(\vec{z}, \hat{q}), \mathbf{u}_p^h)_{L_{\hat{d}}} \in \mathbb{C}. \tag{4.7}$$

If we denote with F the corresponding noise-free version of F^h, by using representation (4.6) for F^h and the analogous one for F, we can easily prove that

$$\|\mathsf{F}^h - \mathsf{F}\| = \|\mathcal{F}^h - \mathcal{F}\| = |\sigma_0^h - \sigma_0| \leq h, \tag{4.8}$$

where σ_0 is the largest singular value of $\mathcal{F}$: this means that the bounds on the levels of noise affecting $\mathcal{F}^h$ and F^h are the same, i.e. equal to h.

We can now use the operator F^h to collect the infinitely many algebraic systems (4.1) into the following single functional equation, written in $[L^2(\mathcal{B})]^{2L_{\hat{x}}}$ for the unknown $\mathbf{G}(\cdot) \in [L^2(\mathcal{B})]^{2L_{\hat{d}}}$:

$$[\mathsf{F}^h\mathbf{G}(\cdot)](\cdot) = \mathbf{E}_{e,\infty}(\cdot), \tag{4.9}$$

where $\mathbf{E}_{e,\infty}(\cdot)$ is the element of $[L^2(\mathcal{B})]^{2L_{\hat{x}}}$ obtained from $\mathbf{E}_{e,\infty}(\vec{z}, \hat{q})$ by simply regarding the sampling pair $(\vec{z}, \hat{q})$ as a variable on $\mathcal{B}$. It is now clear that the regularization of the previous equation (4.9) requires a single-step procedure, thus providing a single value α^* for the regularization parameter, which is independent of both $\vec{z}$ and $\hat{q}$ (however, in general, α^* may depend on the choice of the investigation domain T). Then, the next problem to be solved is how to compute the Tikhonov regularized solution of equation (4.9): this task is accomplished by the following theorem, which shows that, for a generic α, both the generalized and the regularized solutions of (4.9) are obtained from the generalized and regularized solutions of (4.1) by simply regarding the sampling pair $(\vec{z}, \hat{q})$ as a variable on $\mathcal{B}$.

Theorem 4.3: *The generalized and Tikhonov regularized solutions of equation* (4.9) *are given by*

$$\mathbf{G}^{h\dagger}(\cdot) = \sum_{p=0}^{r^h-1} \frac{1}{\sigma_p^h} \left(\mathbf{E}_{e,\infty}(\cdot), \mathbf{v}_p^h\right)_{L_{\hat{x}}} \mathbf{u}_p^h \tag{4.10}$$

and

$$\mathbf{G}_\alpha(\cdot) = \sum_{p=0}^{r^h-1} \frac{\sigma_p^h}{(\sigma_p^h)^2 + \alpha} \left(\mathbf{E}_{e,\infty}(\cdot), \mathbf{v}_p^h\right)_{L_{\hat{x}}} \mathbf{u}_p^h. \tag{4.11}$$

Proof. We prove the result for the generalized solution (the result for the Tikhonov regularized solution can be shown in an analogous way). Since the generalized solution $\mathbf{G}^{h\dagger}(\vec{z},\hat{q})$ of equation (4.1) is its (unique) least-squares solution of minimum norm, then for any $\mathbf{G}(\cdot)$ in $[L^2(\mathcal{B})]^{2L_{\hat{d}}}$ and for almost all $(\vec{z},\hat{q})\in\mathcal{B}$ it holds:

$$\left\|\mathbf{F}^h\mathbf{G}^{h\dagger}(\vec{z},\hat{q})-\mathbf{E}_{e,\infty}(\vec{z},\hat{q})\right\|^2_{L_{\hat{x}}}\leq\left\|\mathbf{F}^h\mathbf{G}(\vec{z},\hat{q})-\mathbf{E}_{e,\infty}(\vec{z},\hat{q})\right\|^2_{L_{\hat{x}}}, \tag{4.12}$$

and then

$$\int_{\mathcal{B}}\left\|\mathbf{F}^h\mathbf{G}^{h\dagger}(\vec{z},\hat{q})-\mathbf{E}_{e,\infty}(\vec{z},\hat{q})\right\|^2_{L_{\hat{x}}}d\vec{z}\,ds(\hat{q})\leq\int_{\mathcal{B}}\left\|\mathbf{F}^h\mathbf{G}(\vec{z},\hat{q})-\mathbf{E}_{e,\infty}(\vec{z},\hat{q})\right\|^2_{L_{\hat{x}}}d\vec{z}\,ds(\hat{q}). \tag{4.13}$$

It is now useful to observe that, by virtue of definition (4.4), for any $\mathbf{G}(\cdot)$ in $[L^2(\mathcal{B})]^{2L_{\hat{d}}}$ it holds:

$$\mathbf{F}^h\mathbf{G}(\vec{z},\hat{q})=[\mathsf{F}^h\mathbf{G}(\cdot)](\vec{z},\hat{q}); \tag{4.14}$$

as a consequence, we can rewrite the previous inequality (4.13) as

$$\begin{aligned}\int_{\mathcal{B}}\left\|\left[\mathsf{F}^h\mathbf{G}^{h\dagger}(\cdot)\right](\vec{z},\hat{q})-\mathbf{E}_{e,\infty}(\vec{z},\hat{q})\right\|^2_{L_{\hat{x}}}d\vec{z}\,ds(\hat{q})\leq\\ \leq\int_{\mathcal{B}}\left\|\left[\mathsf{F}^h\mathbf{G}(\cdot)\right](\vec{z},\hat{q})-\mathbf{E}_{e,\infty}(\vec{z},\hat{q})\right\|^2_{L_{\hat{x}}}d\vec{z}\,ds(\hat{q}),\end{aligned} \tag{4.15}$$

having denoted with $\mathbf{G}^{h\dagger}(\cdot)$ the element in $[L^2(\mathcal{B})]^{2L_{\hat{d}}}$ defined in (4.10) and simply obtained from $\mathbf{G}^{h\dagger}(\vec{z},\hat{q})$ when the sampling pair $(\vec{z},\hat{q})$ is regarded as a variable on $\mathcal{B}$. Recalling definition (4.3) and considering its analogous for $[L^2(\mathcal{B})]^{2L_{\hat{x}}}$, we can rewrite inequality (4.15) as

$$\left\|\left[\mathsf{F}^h\mathbf{G}^{h\dagger}(\cdot)\right](\cdot)-\mathbf{E}_{e,\infty}(\cdot)\right\|^2_{2,L_{\hat{x}}}\leq\left\|\left[\mathsf{F}^h\mathbf{G}(\cdot)\right](\cdot)-\mathbf{E}_{e,\infty}(\cdot)\right\|^2_{2,L_{\hat{x}}}, \tag{4.16}$$

whence we immediately get

$$\mathbf{G}^{h\dagger}(\cdot)=\operatorname{argmin}\left\|\left[\mathsf{F}^h\mathbf{G}(\cdot)\right](\cdot)-\mathbf{E}_{e,\infty}(\cdot)\right\|^2_{2,L_{\hat{x}}}, \tag{4.17}$$

since inequality (4.16) holds for all $\mathbf{G}(\cdot)$ in $[L^2(\mathcal{B})]^{2L_{\hat{d}}}$.

Relation (4.17) states that $\mathbf{G}^{h\dagger}(\cdot)$ is a least-squares solution of equation (4.9); to show that its norm is minimum (and, consequently, that it is the generalized solution of (4.9)), we recall that $\mathbf{G}^{h\dagger}(\vec{z},\hat{q})\in\mathcal{N}(\mathbf{F}^h)$ for all $(\vec{z},\hat{q})$ in $\mathcal{B}$: then, by virtue of statement iii) in Theorem 4.2, we find that $\mathbf{G}^{h\dagger}(\cdot)\in\mathcal{N}(\mathsf{F}^h)$. This concludes the proof. □

The final step is now to fix the optimal value of the regularization parameter α, which, in expression (4.11), is still generic. This task can be accomplished by using the generalized discrepancy principle in the new functional context, i.e. by finding the zero of the new generalized discrepancy function

$$\rho(\alpha)=\left\|\left[\mathsf{F}^h\mathbf{G}_\alpha(\cdot)\right](\cdot)-\mathbf{E}_{e,\infty}(\cdot)\right\|^2_{2,L_{\hat{x}}}-h^2\|\mathbf{G}_\alpha(\cdot)\|^2_{2,L_{\hat{d}}}, \tag{4.18}$$

which, by virtue of (4.3), (4.6) and (4.11), can be written as

$$\rho(\alpha) = \sum_{p=0}^{r^h-1} \frac{\alpha^2 - h^2(\sigma_p^h)^2}{[\alpha + (\sigma_p^h)^2]^2} \int_{\mathcal{B}} \left| \left(\mathbf{E}_{e,\infty}(\vec{z}, \hat{q}) \, , \, \mathbf{v}_p^h \right)_{L_{\hat{x}}} \right|^2 d\vec{z}\, ds(\hat{q}). \tag{4.19}$$

It is very easy to prove that the solution of the equation $\rho(\alpha) = 0$ belongs to the interval $[h\sigma^h_{r^h-1}, h\sigma^h_0]$: this information can be useful when the solution is numerically computed. Moreover, remembering that $\mathcal{B} = T \times \Omega$ and exploiting the linearity of $\mathbf{E}_{e,\infty}(\vec{z}, \hat{q})$ with respect to $\hat{q}$ (see (2.9), (3.9), (3.24)), it follows that

$$\int_{\mathcal{B}} \left| \left(\mathbf{E}_{e,\infty}(\vec{z}, \hat{q}) \, , \, \mathbf{v}_p^h \right)_{L_{\hat{x}}} \right|^2 d\vec{z}\, ds(\hat{q}) = \frac{4\pi}{3} \sum_{j=1}^{3} \int_T \left| \left(\mathbf{E}_{e,\infty}(\vec{z}, \hat{e}_j) \, , \, \mathbf{v}_p^h \right)_{L_{\hat{x}}} \right|^2 d\vec{z}, \tag{4.20}$$

where $\{\hat{e}_j \, : \, j = 1, 2, 3\}$ is the canonical basis of $\mathbb{R}^3$. Now, taking into account the explicit expression of $\mathbf{E}_{e,\infty}(\vec{z}, \hat{q})$, as given by (2.9), (3.9) and (3.24), we can analytically compute the integral on T appearing in equality (4.20). To this end, for any $j \in \{1, 2, 3\}$ we introduce the complex vector $\mathbf{w}_j \in \mathbb{C}^{L_{\hat{x}}}$ whose $\ell_{\hat{x}}$-th component, $\forall \ell_{\hat{x}} = 0, \ldots, L_{\hat{x}} - 1$, is defined as

$$\begin{aligned} w_{j,\ell_{\hat{x}}} := {} & v^h_{p,\ell_{\hat{x}}} \Delta s_{\ell_{\hat{x}}} [(\hat{x}_{\ell_{\hat{x}}} \times \hat{e}_j) \times \hat{x}_{\ell_{\hat{x}}}] \cdot \hat{\theta}(\hat{x}_{\ell_{\hat{x}}}) + \\ & + v^h_{p,\ell_{\hat{x}}+L_{\hat{x}}} \Delta s_{\ell_{\hat{x}}} [(\hat{x}_{\ell_{\hat{x}}} \times \hat{e}_j) \times \hat{x}_{\ell_{\hat{x}}}] \cdot \hat{\varphi}(\hat{x}_{\ell_{\hat{x}}}), \end{aligned} \tag{4.21}$$

where $v^h_{p,\ell_{\hat{x}}}$ is the $\ell_{\hat{x}}$-th component of the singular vector $\mathbf{v}_p^h \in \mathbb{C}^{2L_{\hat{x}}}$, $\Delta s_{\ell_{\hat{x}}}$ is defined at the end of Remark 3.1 and $\hat{x}_{\ell_{\hat{x}}}$ is given by (3.14); then, a simple computation leads to

$$\int_T \left| \left(\mathbf{E}_{e,\infty}(\vec{z}, \hat{e}_j) \, , \, \mathbf{v}_p^h \right)_{L_{\hat{x}}} \right|^2 d\vec{z} = \mathbf{w}_j^{\mathrm{T}} \mathbf{S}\, \overline{\mathbf{w}}_j, \tag{4.22}$$

where $\mathbf{S}$ is the square real matrix of $L_{\hat{x}} \times L_{\hat{x}}$ elements defined as

$$\mathbf{S}_{\ell^1_{\hat{x}} \ell^2_{\hat{x}}} := \frac{k^2}{2\pi^2} \prod_{j=1}^{3} A_j \, \mathrm{sinc} \left[\frac{kA_j}{\pi} \left(\hat{x}_{\ell^1_{\hat{x}}} - \hat{x}_{\ell^2_{\hat{x}}} \right) \cdot \hat{e}_j \right] \quad \forall \ell^1_{\hat{x}}, \ell^2_{\hat{x}} = 0, \ldots, L_{\hat{x}} - 1. \tag{4.23}$$

We recall that in equality (4.23) the positive numbers A_j are the half-lengths of the sides of the parallelepiped $T = \prod_{j=1}^{3} [-A_j, A_j]$ representing our domain of investigation. Hence, from equations (4.20) and (4.22) it follows that

$$\int_{\mathcal{B}} \left| \left(\mathbf{E}_{e,\infty}(\vec{z}, \hat{q}) \, , \, \mathbf{v}_p^h \right)_{L_{\hat{x}}} \right|^2 d\vec{z}\, ds(\hat{q}) = \frac{4\pi}{3} \sum_{j=1}^{3} \mathbf{w}_j^{\mathrm{T}} \mathbf{S}\, \overline{\mathbf{w}}_j. \tag{4.24}$$

By inserting this result into (4.19), we obtain for the generalized discrepancy $\rho(\alpha)$ an explicit analytical expression allowing a very fast computation of its zero α^*; by using such value for the regularization parameter α in (4.11), we find the following representation for the optimal regularized solution of the functional problem (4.9):

$$\mathbf{G}_{\alpha^*}(\cdot) = \sum_{p=0}^{r^h-1} \frac{\sigma_p^h}{(\sigma_p^h)^2 + \alpha^*} \left(\mathbf{E}_{e,\infty}(\cdot), \mathbf{v}_p^h \right)_{L_{\hat{x}}} \mathbf{u}_p^h. \tag{4.25}$$

The most general indicator function we can now consider is $J(\Psi)$, where $J : [0, +\infty) \to \mathbb{R}$ is an appropriate monotonic function and

$$\Psi(\vec{z}) := \int_\Omega \|\mathbf{G}_{\alpha^*}(\vec{z}, \hat{q})\|^2_{L_{\hat{x}}} \, ds(\hat{q}) = \\ = \frac{4\pi}{3} \sum_{j=1}^{3} \sum_{p=0}^{r^h-1} \frac{(\sigma_p^h)^2}{[(\sigma_p^h)^2 + \alpha^*]^2} \left| \left(\mathbf{E}_{e,\infty}(\vec{z}, \hat{e}_j), \mathbf{v}_p^h \right)_{L_{\hat{x}}} \right|^2 \quad \forall \vec{z} \in T. \tag{4.26}$$

The analytic form (4.26) of Ψ, which represents the core of the indicator function, justifies the name "no-sampling" for our approach: indeed, α^* does not depend on the sampling pair $(\vec{z}, \hat{q})$, the term $\mathbf{E}_{e,\infty}(\vec{z}, \hat{e}_j)$ is analytically known and the singular system $\{\sigma_p^h, \mathbf{u}_p^h, \mathbf{v}_p^h\}_{p=0}^{r^h-1}$ of the operator $\mathcal{F}^h$ is determined from the far-field patterns measured. Moreover, as highlighted by (4.20) and (4.26), in our approach the three independent polarizations $\hat{e}_j$ naturally play an equally important role in forming the indicator function: as a consequence, the heuristic procedure adopted in [8] to average the contributions of the three polarizations $\hat{e}_j$ is automatically incorporated in the new rigorous formalism.

Of course, Theorem 4.3 now inspires a new implementation of the linear sampling method, whereby the contour of the scatterer is detected by all points in which the indicator function $J(\Psi)$ becomes mostly large or small, depending on the choice of J.

5. Numerical applications

In this section we want to show that our no-sampling implementation yields reconstructions that are very similar to those obtained by means of the traditional approach based on a sampling in the physical and polarization spaces, but in an extremely reduced amount of time and in a completely automatic fashion. In general, the 3D reconstruction of the scatterer is obtained by plotting the C–level surface of the indicator function $J(\Psi)$, i.e. the surface described by the Cartesian equation

$$J[\Psi(\vec{z})] = C, \qquad \vec{z} \in T, \tag{5.1}$$

where $C \in [\min_{\vec{z}\in T} J[\Psi(\vec{z})], \max_{\vec{z}\in T} J[\Psi(\vec{z})]]$ is set to obtain the optimal visualization. Our aim is now to give a recipe to fix in an automatic way the C–level surface of $J(\Psi)$. An effective approach is the following three-step algorithm.

(i) Consider the 2D indicator function $J(\beta)$, where β is the 2D map

$$\beta : \mathbb{R}^2 \ni (u_1, u_2) \mapsto \Psi[\xi(u_1, u_2)] \in \mathbb{R} \tag{5.2}$$

and $\xi : \mathbb{R}^2 \ni (u_1, u_2) \mapsto (a_{11}u_1 + a_{12}u_2 + c_1, a_{21}u_1 + a_{22}u_2 + c_2, a_{31}u_1 + a_{32}u_2 + c_3) \in \mathbb{R}^3$ is the parametric equation of a plane in $\mathbb{R}^3$ containing a slice of the scatterer; such a plane can be found by using the (rather weak) a priori information on the scatterer suggesting where the scatterer is in the imaging volume.

(ii) Apply an active contour technique to $J(\beta)$ as in [2], i.e. find a plane curve of parametric equation $\gamma : [0,1] \to \mathbb{R}^2$ minimizing the energy functional

$$\mathcal{E}(\gamma) := \int_0^1 \left[\frac{1}{2} \left(w_1(s) \|\gamma'(s)\|_{\mathbb{R}^2} + w_2(s) \|\gamma''(s)\|_{\mathbb{R}^2} \right) + E_{ext}(\gamma(s)) \right] ds, \quad (5.3)$$

where

$$E_{ext} := - \|\nabla J(\beta)\|^2_{\mathbb{R}^2} . \quad (5.4)$$

(iii) Since active contours generate profiles that are close to level curves, the value of the indicator function on one of these profiles is almost constant. Therefore we choose

$$C := \int_0^1 J \left\{ \Psi \left[\xi(\gamma^\star(t)) \right] \right\} \, dt \quad (5.5)$$

with $\gamma^\star = \operatorname{argmin}_\gamma \mathcal{E}(\gamma)$, i.e. the mean value of $J(\Psi)$ evaluated over the points of $\xi(\gamma^\star)$.

The computation of the active contour in step (ii) is accomplished as in [2, 5]. The external force in (5.4) can be determined by computing $\nabla J(\beta)$ numerically or analytically: in the former approach, starting from the knowledge of $J(\beta)$ on a prefixed grid of points, the gradient $\nabla J(\beta)$ is computed once for all on the same grid by means of finite differences and used (with interpolation) to deform the contours obtained at each iteration, while in the latter the knowledge of the analytical form of the indicator function $J(\Psi)$ allows computing the numerical value of $\nabla J(\beta)$ time by time on a finite number of points exactly belonging to the contours obtained at each iteration. For the reconstructions in the present paper we tested both procedures, but since the differences in the visualization quality are negligible, we shall illustrate only the results obtained when $\nabla J(\beta)$ is computed by means of finite differences: indeed, the latter procedure turns out to be faster, owing to the analytical form of $\nabla J(\beta)$, which is now more complicated than in the genuine 2D case discussed in [2].

Remark 5.1. The previous three-step algorithm can be in principle implemented even for traditional linear sampling: however, in this case the determination of C through (5.5) would require a notably greater computational effort. Indeed, in general, the 3D grid $\mathcal{Z}$ of sampling points $\vec{z}$ on which the indicator function $J(\Psi)$ is computed has nothing to do with the 2D grid $\mathcal{G}$ used to implement the active contour technique on a plane section of the scatterer: as a consequence, $J(\Psi)$ should be computed also on $\mathcal{G}$, then the final contour resulting from the edge detection technique should be either

deformed by interpolation and discretized on a proper number of points belonging to $\mathcal{G}$ itself, or even discretized in an ad-hoc set of points, on which $J(\Psi)$ should be computed separately. If we now remember that in the traditional implementation of the linear sampling method the regularization procedure needs to be repeated for each sampling pair $(\vec{z}, \hat{q})$, we can easily understand that this approach is rather heavy from a computational viewpoint.

We now present and discuss three numerical experiments: in each one of them, the discretization described in Section 3 is adopted by using the same uniform 9×18 angular mesh on the unit sphere for both the observation and the incidence directions: more precisely, we choose the observation angles $\theta_i^{\hat{x}} = \dfrac{\pi}{T_{\hat{x}}}\left(i + \dfrac{1}{2}\right)$ for all $i = 0, \ldots, T_{\hat{x}} - 1$ with $T_{\hat{x}} = 9$ and $\varphi_j^{\hat{x}} = \dfrac{2\pi}{F_{\hat{x}}} j$ for all $j = 0, \ldots, F_{\hat{x}} - 1$ with $F_{\hat{x}} = 18$, and the incidence angles $\theta_i^{\hat{d}} = \dfrac{\pi}{T_{\hat{d}}}\left(i + \dfrac{1}{2}\right)$ for all $i = 0, \ldots, T_{\hat{d}} - 1$ with $T_{\hat{d}} = 9$ and $\varphi_j^{\hat{d}} = \dfrac{2\pi}{F_{\hat{d}}} j$ for all $j = 0, \ldots, F_{\hat{d}} - 1$ with $F_{\hat{d}} = 18$. The far-field patterns forming the matrix $\mathbf{E}_\infty$ defined in (3.25) are computed by using a code based on the method of moments; each entry of $\mathbf{E}_\infty$ is then affected by 7% Gaussian noise. The scatterers are all isotropic and located in vacuum: this means that the index of refraction is given by

$$N(\vec{x}) = n(\vec{x}) I, \tag{5.6}$$

$$n(\vec{x}) = \frac{1}{\epsilon_0}\left[\epsilon_r(\vec{x}) + \mathrm{i}\frac{\sigma(\vec{x})}{\omega}\right], \tag{5.7}$$

where I is the 3×3 identity matrix, ϵ_0 is the dielectric constant in vacuum, $\epsilon_r(\vec{x})$ and $\sigma(\vec{x})$ are the relative permittivity and the conductivity of the scatterer at the point $\vec{x}$, and finally $\omega = 2\pi\nu$ is the angular frequency. All no-sampling visualizations are realized by choosing $J(t) = t^{-1}\ \forall t \in \mathbb{R}^+ \cup \{0\}$ and taking as domain of investigation a cube of side 3 m, i.e. $T = [-1.5, 1.5]^3$. In all the numerical tests, the forward scattering problem has been solved by using a stabilized biconjugated-gradient fast Fourier transform (BCGS-FFT) method of moments code [18]. The computation domain has been discretized into cubical subdomains of side about $\lambda/20$, being λ the wavelength of the incident field in vacuum.

The first numerical example we consider is the reconstruction of the "U-shaped" scatterer in Figure 1(a): this object is characterized by constant $\epsilon_r = 1.8$ and $\sigma = 0.02$ S·m^{-1}. The frequency used to perform this experiment is $\nu = 300$ MHz, corresponding to a wavelength $\lambda = 1.0$ m in vacuum. In order to determine the threshold value C in equation (5.1), we follow the previously described scheme. More precisely, if we refer

$\mathbb{R}^3$ to the usual Cartesian coordinate system (x_1, x_2, x_3), as shown in Figure 1(a), we restrict the indicator function $J(\Psi)$ to the plane of Cartesian equation $x_2 = 0$; an axial view of the 2D map visualizing this restriction is represented in Figure 1(b). Then, the active contour technique is applied to the previous visualization map starting from a suitable initial guess (the white circle in Figure 1(b)), and the converging profile (also shown in Figure 1(b) as a black line) is used as the argument of the function $J\{\Psi[\xi(\cdot)]\}$ in equation (5.5). The resulting estimate of C is inserted into equation (5.1) and the corresponding reconstruction of the scatterer, represented in Figure 1(c), is obtained after 90.1 s of computation time with a 1.6 GHz CPU. In Figure 1(d) we show the reconstruction provided by the traditional implementation of the linear sampling method (as explained in [8]) after 1590.1 s of computation time: in this case we have uniformly discretized the investigation domain T with a sampling grid $\mathcal{Z}$ of $30 \times 30 \times 30$ points and combined the three indicator functions corresponding to the three independent polarizations $\hat{e}_1 = (1, 0, 0)$, $\hat{e}_2 = (0, 1, 0)$, $\hat{e}_3 = (0, 0, 1)$; different cut-off values C have been used until the "best visual reconstruction", shown in Figure 1(d), has been obtained. The only difference with respect to [8] is that here, in order to make a consistent comparison with our no-sampling indicator function $J(\Psi) = 1/\Psi$, we choose

$$\Theta(\vec{z}) := \left[\frac{1}{3}\sum_{j=1}^{3}\left\|\mathbf{G}_{\vec{z},\hat{e}_j;\,\alpha^*(\vec{z},\hat{e}_j)}\right\|^2_{L_{\hat{d}}}\right]^{-1} \qquad \forall \vec{z} \in \mathcal{Z} \tag{5.8}$$

as sampled indicator function, instead of

$$\Theta(\vec{z}) := \frac{1}{3}\sum_{j=1}^{3}\left\|\mathbf{G}_{\vec{z},\hat{e}_j;\,\alpha^*(\vec{z},\hat{e}_j)}\right\|^{-1}_{L_{\hat{d}}} \qquad \forall \vec{z} \in \mathcal{Z}, \tag{5.9}$$

where $\left\|\mathbf{G}_{\vec{z},\hat{e}_j;\,\alpha^*(\vec{z},\hat{e}_j)}\right\|^2_{L_{\hat{d}}}$ is given by (3.33) for each $j \in \{1, 2, 3\}$.

The following three considerations must be accounted for:

- all the input parameters in the active contour algorithm are optimally fixed by choosing them in the ranges that, according to the theory, assure the convergence of the iteration (see [5]);
- the reconstruction in Figure 1(c) provided by the no-sampling formulation coupled with deformable models is less accurate than the reconstruction in Figure 1(d) provided by linear sampling coupled with a heuristic choice of the threshold value C based on a visual comparison with the true scatterer (supposed known). However, as many numerical tests proved, this difference in accuracy is not due to no-sampling but to a non-optimal performance of the edge detection technique employed: indeed, applying heuristic thresholding to no-sampling would lead to reconstructions more or less identical to those provided by traditional linear sampling;
- in the overall computational time of the no-sampling implementation, most of the

time (around 80 s) is spent for the edge detection procedure in Figure 1(b) and for the visualization process, while the determination of the unique regularization parameter only takes around 2 s. On the contrary, in the sampling formulation most of the time is devoted to the construction of the indicator function.

The second test is concerned with the non-connected scatterer in Figure 2(a), characterized by constant $\epsilon_r = 2.0$ and $\sigma = 0.0$ S m^{-1} for both the U-forms and the sphere in between. The frequency chosen for this experiment is $\nu = 286$ MHz, corresponding to a wavelength $\lambda = 1.05$ m in vacuum. The scatterer is firstly cut by the plane in $\mathbb{R}^3$ of Cartesian equation $x_2 = 0.9$ and the usual deformable model is applied to the corresponding visualization shown in Figure 2(b) together with the initial guess (white ellipse) and the reconstructed profile (black contour). The cut-off value C is then computed by means of equation (5.5) and the resulting surface (5.1) is plotted in Figure 2(c). In Figure 2(d) we show the result obtained by using the traditional linear sampling with the same choices for the parameters and the indicator function and the same heuristic procedure for estimating C as in the previous numerical experiment. The computational times for both reconstructions are around the same ones as for the corresponding reconstructions in Figure 1.

Finally, the third numerical experiment is performed by using the non-connected scatterer in Figure 3(a) at a frequency $\nu = 300$ MHz: the parallelepiped on the left is centred in $(-0.75, 0, 0)$ and characterized by constant $\epsilon_r = 2.1$ and $\sigma = 0.0$ S m^{-1}, while that on the right is centred in $(0.75, 0, 0)$ and characterized by constant $\epsilon_r = 1.5$ and $\sigma = 0.0$ S m^{-1}. In this case we only adopt the no-sampling approach, but with three different strategies. In the first strategy, the scatterer is cut by the plane $x_1 = -0.75$ and the threshold C is determined as usual to obtain the reconstruction in Figure 3(b). In the second strategy, we use the plane $x_1 = 0.75$, which provides the reconstruction in Figure 3(c). Finally, if we split the domain of investigation T into $T_1 := [-1.5, 0] \times [-1.5, 1.5] \times [-1.5, 1.5]$ and $T_2 := [0, 1.5] \times [-1.5, 1.5] \times [-1.5, 1.5]$, intersect T_1 with $x_1 = -0.75$, T_2 with $x_1 = 0.75$ and use the two corresponding threshold values to reconstruct the two objects with different ϵ_r, we obtain the reconstruction shown in Figure 3(d): this last procedure allows better preserving the original size of the two objects in the non-connected scatterer.

As a final comment, we observe that it is certainly possible to consider scatterers which are much more complex than those chosen here to illustrate the advantages of the no-sampling formulation of the linear sampling method: for example, we could consider anisotropic, inhomogeneous and non-connected scatterers, with connected components that are very close to each other (with respect to the wavelength λ) and, consequently, hard to separate in the reconstruction. In these very general cases, the most suitable approach for post-processing the indicator function is probably an iterative procedure based on level sets (see [16] and references therein): indeed, level sets can easily detect

non-connected objects starting from a connected initial guess, since their formulation (unlike the active contour technique used in this paper) enables an automatic splitting of the profiles obtained during the iterations; moreover, the final visualization provided by such a procedure does not need to be a level surface of the indicator function, thus allowing a more reliable reconstruction of strongly inhomogeneous and non-connected scatterers. Implementing a level-set-based technique for a post-processing of the no-sampling linear sampling is beyond the purposes of this paper; however, we point out that, in principle, the analytical knowledge of the indicator function can be very useful also for such a technique.

6. Conclusions

In this paper we have introduced a no-sampling version of the linear sampling method for 3D electromagnetic inverse scattering problems. In this approach the availability of an analytically known indicator function allows the fast and automatic visualization of the scatterers from the knowledge of their far-field patterns. Possible open problems are concerned with the assessment of the spatial resolution achievable with the method and its effectiveness in the case of limited aperture data.

Appendix

Let M and N be two positive integers; let the $M \times M$ matrix $\mathbf{\Delta S}_M$ and the $N \times N$ matrix $\mathbf{\Delta S}_N$ be diagonal and positive-definite; let the vector spaces $\mathbb{C}^M$ and $\mathbb{C}^N$ be equipped with the scalar products $(\cdot,\cdot)_{\mathbf{\Delta S}_M}$ and $(\cdot,\cdot)_{\mathbf{\Delta S}_N}$ described by $\mathbf{\Delta S}_M$ and $\mathbf{\Delta S}_N$ respectively, i.e.:

$$(\mathbf{x}_1, \mathbf{x}_2)_{\mathbf{\Delta S}_M} := \mathbf{x}_1^{\mathrm{T}} \mathbf{\Delta S}_M \overline{\mathbf{x}}_2, \qquad (\mathbf{y}_1, \mathbf{y}_2)_{\mathbf{\Delta S}_N} := \mathbf{y}_1^{\mathrm{T}} \mathbf{\Delta S}_N \overline{\mathbf{y}}_2, \tag{A1}$$

where $\mathbf{x}_1, \mathbf{x}_2 \in \mathbb{C}^M$ and $\mathbf{y}_1, \mathbf{y}_2 \in \mathbb{C}^N$ are generic column vectors. Let the linear operator $\mathcal{T} : \left(\mathbb{C}^M, (\cdot,\cdot)_{\mathbf{\Delta S}_M}\right) \to \left(\mathbb{C}^N, (\cdot,\cdot)_{\mathbf{\Delta S}_N}\right)$ be represented by the $N \times M$ matrix $\mathbf{T}$. We denote with $(\mathbf{\Sigma}, \mathbf{U}, \mathbf{V})$ the singular system of $\mathcal{T}$, such that

$$\mathbf{T}\mathbf{U} = \mathbf{V}\mathbf{\Sigma}, \qquad \mathbf{T}^* \mathbf{V} = \mathbf{U}\mathbf{\Sigma} \tag{A2}$$

with the othonormality properties

$$\mathbf{U}^{\mathrm{T}} \mathbf{\Delta S}_M \overline{\mathbf{U}} = \mathbf{I}_r, \qquad \mathbf{V}^{\mathrm{T}} \mathbf{\Delta S}_N \overline{\mathbf{V}} = \mathbf{I}_r, \tag{A3}$$

where $\mathbf{I}_r$ is the $r \times r$ identity matrix, r is the rank of $\mathbf{T}$ and $\mathbf{T}^*$ is the matrix representing the adjoint operator $\mathcal{T}^*$. Then the following theorem holds.

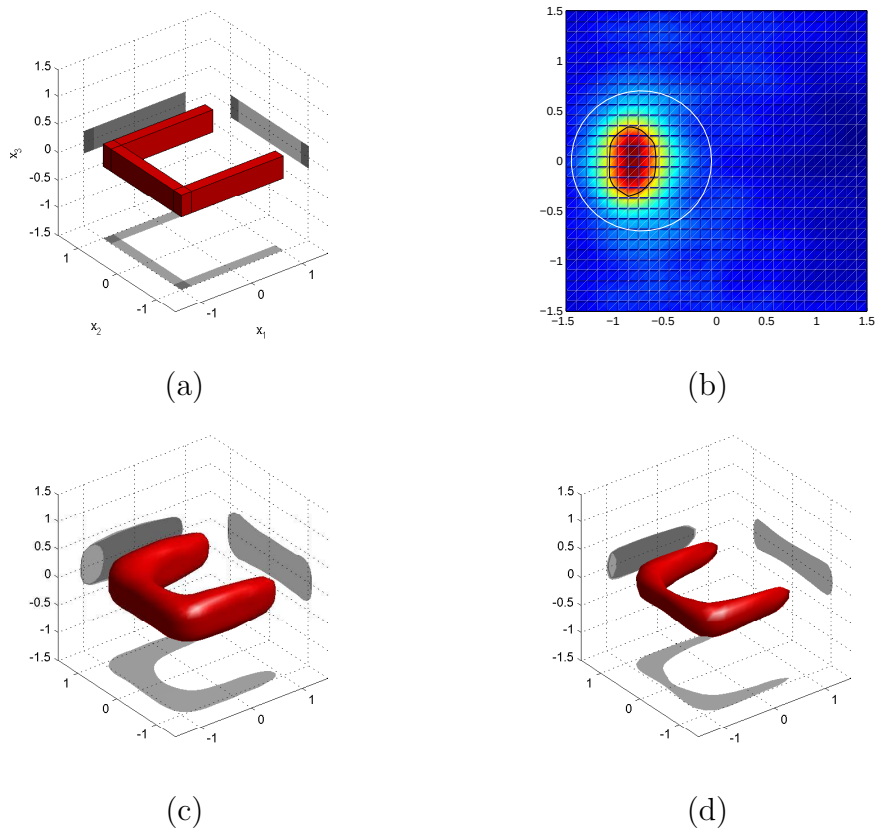

Figure 1. Reconstruction effectiveness of 3D no-sampling linear sampling: (a) the scattering object; (b) application of active contours to the restriction of the indicator function to $x_2 = 0$ (white line: initialization; black line: final profile); (c) reconstruction provided by no-sampling linear sampling in around 90 s of CPU time (the threshold value for the surface equation is computed by using (5.5)); (d) reconstruction provided by traditional linear sampling in around 1600 s of CPU time (the threshold value for the surface equation is obtained by means of a heuristic trial-and-error procedure).

Theorem A.1. *Let* $\left(\tilde{\boldsymbol{\Sigma}}, \tilde{\mathbf{U}}, \tilde{\mathbf{V}}\right)$ *be the singular system of the matrix*

$$\tilde{\mathbf{T}} := (\boldsymbol{\Delta}\mathbf{S}_N)^{\frac{1}{2}}\, \mathbf{T}\, (\boldsymbol{\Delta}\mathbf{S}_M)^{-\frac{1}{2}}\,. \tag{A4}$$

Then the triple $(\boldsymbol{\Sigma}, \mathbf{U}, \mathbf{V})$ *defined by*

$$\boldsymbol{\Sigma} := \tilde{\boldsymbol{\Sigma}}, \quad \mathbf{U} := (\boldsymbol{\Delta}\mathbf{S}_M)^{-\frac{1}{2}}\, \tilde{\mathbf{U}}, \quad \mathbf{V} := (\boldsymbol{\Delta}\mathbf{S}_N)^{-\frac{1}{2}}\, \tilde{\mathbf{V}} \tag{A5}$$

is the singular system of the operator $\mathcal{T}$*.*

Proof. The fact that $\left(\tilde{\boldsymbol{\Sigma}}, \tilde{\mathbf{U}}, \tilde{\mathbf{V}}\right)$ is the singular system of the matrix $\tilde{\mathbf{T}}$ defined in (A4) means that

$$\tilde{\mathbf{T}}\tilde{\mathbf{U}} = \tilde{\mathbf{V}}\tilde{\boldsymbol{\Sigma}}, \qquad \overline{\tilde{\mathbf{T}}}^{\top}\, \tilde{\mathbf{V}} = \tilde{\mathbf{U}}\tilde{\boldsymbol{\Sigma}} \tag{A6}$$

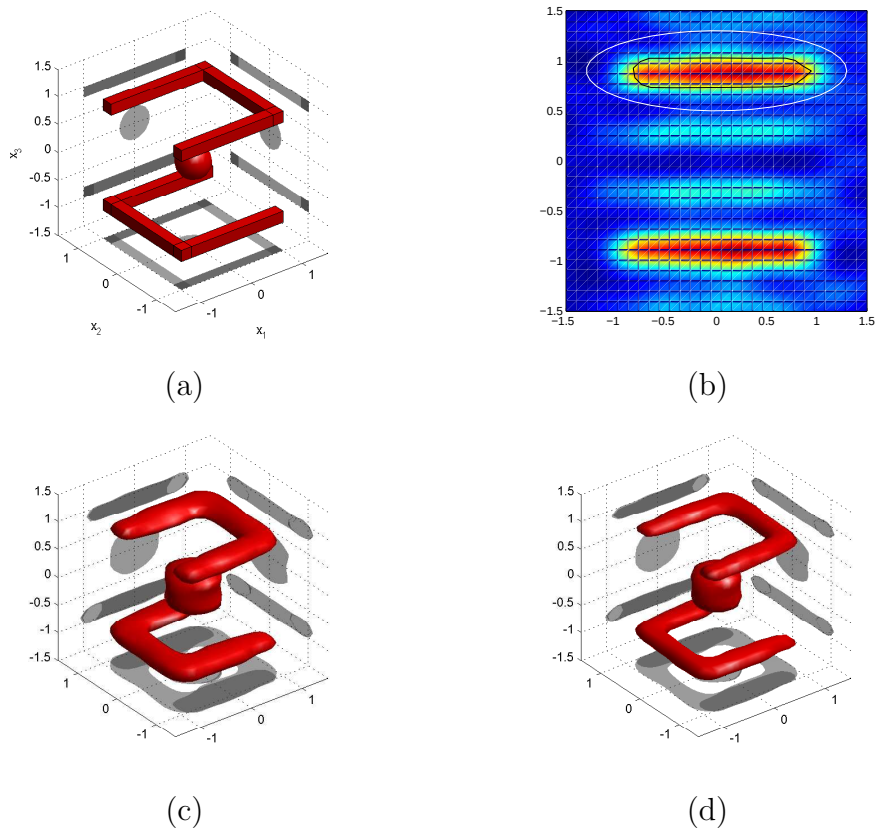

(a) (b)

(c) (d)

Figure 2. Reconstruction effectiveness of 3D no-sampling linear sampling: (a) the scattering object; (b) application of active contours to the restriction of the indicator function to $x_2 = 0.9$ (white line: initialization; black line: final profile); (c) reconstruction provided by no-sampling linear sampling in around 90 s of CPU time (the threshold value for the surface equation is computed by using (5.5)); (d) reconstruction provided by traditional linear sampling in around 1600 s of CPU time (the threshold value for the surface equation is obtained by means of a heuristic trial-and-error procedure).

with the othonormality properties:

$$\tilde{\mathbf{U}}^{\mathrm{T}}\,\overline{\tilde{\mathbf{U}}} = \mathbf{I}_r, \qquad \tilde{\mathbf{V}}^{\mathrm{T}}\,\overline{\tilde{\mathbf{V}}} = \mathbf{I}_r. \tag{A7}$$

Now, by virtue of (A4), (A5), (A6), we have

$$\begin{aligned}\mathbf{T}\mathbf{U} - \mathbf{V}\boldsymbol{\Sigma} &= \mathbf{T}\,(\boldsymbol{\Delta}\mathbf{S}_M)^{-\frac{1}{2}}\,\tilde{\mathbf{U}} - (\boldsymbol{\Delta}\mathbf{S}_N)^{-\frac{1}{2}}\,\tilde{\mathbf{V}}\tilde{\boldsymbol{\Sigma}} = \\ &= (\boldsymbol{\Delta}\mathbf{S}_N)^{-\frac{1}{2}}\left[(\boldsymbol{\Delta}\mathbf{S}_N)^{\frac{1}{2}}\,\mathbf{T}\,(\boldsymbol{\Delta}\mathbf{S}_M)^{-\frac{1}{2}}\,\tilde{\mathbf{U}} - \tilde{\mathbf{V}}\tilde{\boldsymbol{\Sigma}}\right] = \\ &= (\boldsymbol{\Delta}\mathbf{S}_N)^{-\frac{1}{2}}\left[\tilde{\mathbf{T}}\tilde{\mathbf{U}} - \tilde{\mathbf{V}}\tilde{\boldsymbol{\Sigma}}\right] = \mathbf{0},\end{aligned} \tag{A8}$$

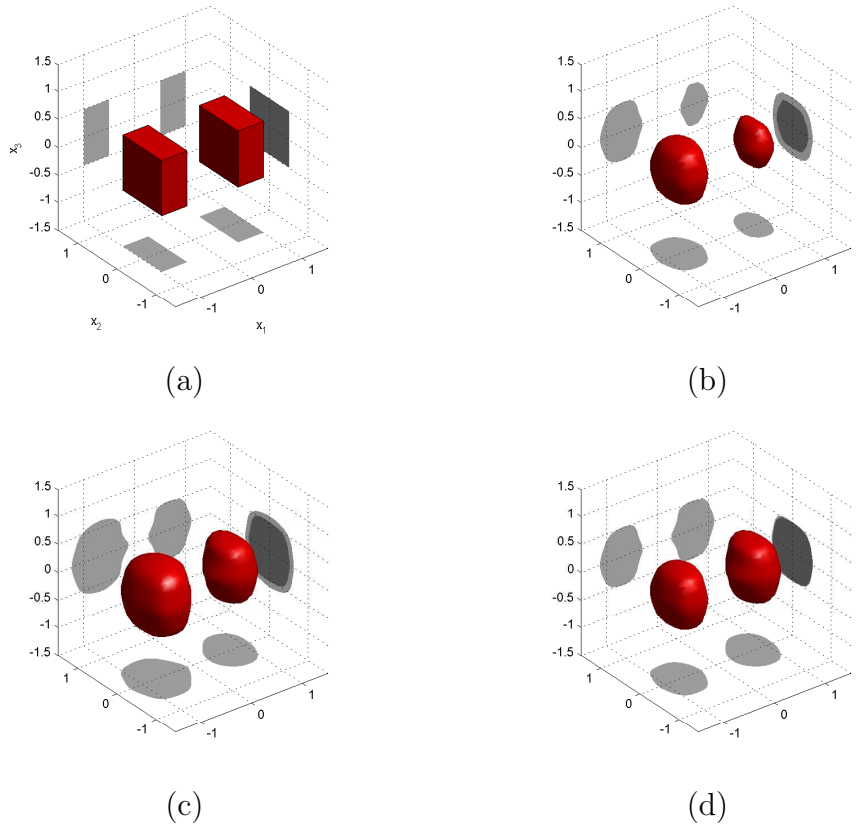

Figure 3. Reconstruction of two objects with different permittivity by means of no-sampling linear sampling: (a) the two scattering objects; (b) reconstruction obtained by choosing a unique threshold value $C = C_1$ computed as in (5.5) by cutting the non-connected scatterer with the plane $x_1 = -0.75$; (c) reconstruction obtained by choosing a unique threshold value $C = C_2$ computed as in (5.5) by cutting the non-connected scatterer with the plane $x_1 = 0.75$; (d) reconstruction obtained by choosing the two different threshold values C_1 and C_2 for visualizing the two objects. The visualization time for each reconstruction is of around 90 s of CPU time.

so that the first of relations (A2) is satisfied. Recalling now (A1), we have:

$$(\mathbf{T}^*\mathbf{y}, \mathbf{x})_{\mathbf{\Delta S}_M} = (\mathbf{T}^*\mathbf{y})^{\mathrm{T}}\, \mathbf{\Delta S}_M \overline{\mathbf{x}} = \mathbf{y}^{\mathrm{T}}\, (\mathbf{T}^*)^{\mathrm{T}}\, \mathbf{\Delta S}_M \overline{\mathbf{x}} \tag{A9}$$

and

$$(\mathbf{y}, \mathbf{T}\mathbf{x})_{\mathbf{\Delta S}_N} = \mathbf{y}^{\mathrm{T}} \mathbf{\Delta S}_N \overline{(\mathbf{T}\mathbf{x})} = \mathbf{y}^{\mathrm{T}} \mathbf{\Delta S}_N \overline{\mathbf{T}}\overline{\mathbf{x}}. \tag{A10}$$

By comparing (A9) with (A10), we find:

$$(\mathbf{T}^*)^{\mathrm{T}}\, \mathbf{\Delta S}_M = \mathbf{\Delta S}_N \overline{\mathbf{T}} \;\Rightarrow\; (\mathbf{T}^*)^{\mathrm{T}} = \mathbf{\Delta S}_N \overline{\mathbf{T}} \mathbf{\Delta S}_M^{-1}, \tag{A11}$$

and then

$$\mathbf{T}^* = \mathbf{\Delta S}_M^{-1}\,\overline{\mathbf{T}}^{\mathrm{T}}\mathbf{\Delta S}_N. \tag{A12}$$

A computation analogous to (A8) now shows that $\mathbf{T}^*\,\mathbf{V}-\mathbf{U}\mathbf{\Sigma} = \mathbf{0}$, i.e. also the second of relations (A2) is satisfied. Finally, the orthonormality properties (A3) are immediately proved by taking into account the analogous properties (A7) and definitions (A5). □

References

[1] Aramini R, Brignone M and Piana M 2006 The linear sampling method without sampling *Inverse Problems* **22** 2237-2254

[2] Aramini R, Brignone M, Coyle J and Piana M 2008 Post-processing of the linear sampling method by means of deformable models SIAM *J. Sci. Comput.* (in press)

[3] Bertero M and Boccacci P 1998 *Introduction to inverse problems in imaging* (Bristol: Institute of Physics Publishing)

[4] Cakoni F and Colton D 2006 *Qualitative methods in inverse scattering theory* (Berlin: Springer)

[5] Cohen L D 1991 On active contour models and balloons CVGIP *Image understanding* **53** 211-218

[6] Cohen L D and Cohen I 1993 Finite-Element Methods for Active Contour Models and Balloons for 2-D and 3-D Images IEEE *Trans. Pattern Anal. Machine Intell.* **15** 1131-1147

[7] Colton D, Haddar H and Monk P 2002 The Linear Sampling Method for Solving the Electromagnetic Inverse Scattering Problem SIAM *J. Sci. Comput.* **24** 719-731

[8] Colton D, Haddar H and Piana M 2003 The linear sampling method in inverse electromagnetic scattering theory *Inverse Problems* **19** S105-S137

[9] Colton D and Kirsch A 1996 A simple method for solving inverse scattering problems in the resonance region *Inverse Problems* **12** 383-393

[10] Colton D and Kress R 1998 *Inverse Acoustic and Electromagnetic Scattering Theory* (Berlin: Springer)

[11] Colton D and Monk P 1998 A linear sampling method for the detection of leukemia using microwaves SIAM *J. Appl. Math.* **58** 926-941

[12] Colton D and Monk P 1998 A linear sampling method for the detection of leukemia using microwaves II SIAM *J. Appl. Math.* **60** 241-255

[13] Colton D, Monk P and Giebermann K 2000 The regularized sampling method SIAM *J. Sci. Comput.* **21** 2316-2330

[14] Colton D and Piana M 1998 The simple method for solving the electromagnetic inverse scattering problem: the case of TE polarized waves *Inverse Problems* **14** 597-614

[15] Colton D, Piana M and Potthast R 1997 A simple method using Morozov's discrepancy principle for solving inverse scattering problems *Inverse Problems* **13** 1477-1493

[16] Sethian J A 1999 *Level Sets Methods and Fast Marching Methods* (Cambridge: Cambridge University Press)

[17] Tikhonov A N, Goncharsky A V, Stepanov V V and Yagola A G 1995 *Numerical Methods for the Solution of Ill-Posed Problems* (Dordrecht: Kluwer)

[18] Zhong Q Z, Qing H L, Xiao C, Ward E, Ybarra G and Joines W T 2003 Microwave Breast Imaging: 3-D Forward Scattering Simulation IEEE *Trans. Biomed. Eng.* **50** 1180-1189